

On the room-temperature phase diagram of high pressure hydrogen: An ab initio molecular dynamics perspective and a diffusion Monte Carlo study

Ji Chen, Xinguo Ren, Xin-Zheng Li, Dario Alfè, and Enge Wang

Citation: *The Journal of Chemical Physics* **141**, 024501 (2014); doi: 10.1063/1.4886075

View online: <http://dx.doi.org/10.1063/1.4886075>

View Table of Contents: <http://scitation.aip.org/content/aip/journal/jcp/141/2?ver=pdfcov>

Published by the [AIP Publishing](#)

Articles you may be interested in

[The different roles of Pu-oxide overlayers in the hydrogenation of Pu-metal: An ab initio molecular dynamics study based on van der Waals density functional \(vdW-DF\)+U](#)

J. Chem. Phys. **140**, 164709 (2014); 10.1063/1.4873418

[Equation of state and phase diagram of ammonia at high pressures from ab initio simulations](#)

J. Chem. Phys. **138**, 234504 (2013); 10.1063/1.4810883

[Constant pressure ab initio molecular dynamics with discrete variable representation basis sets](#)

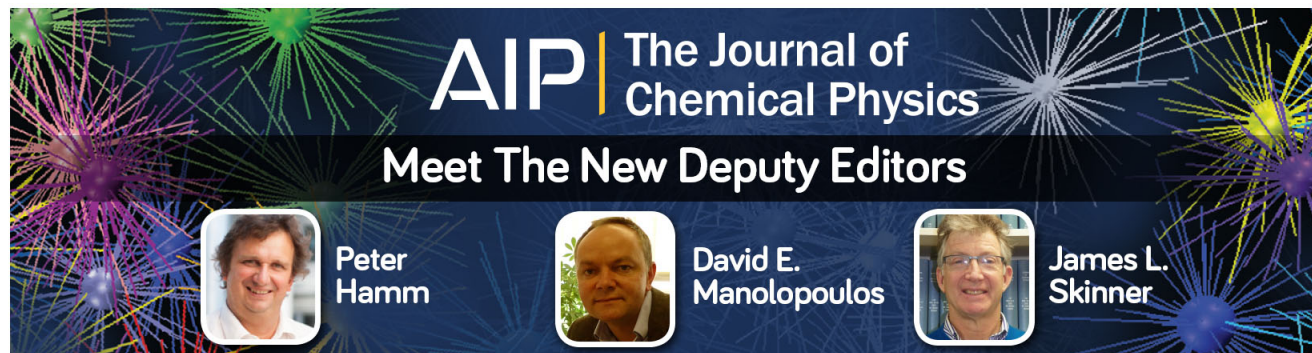
J. Chem. Phys. **133**, 184110 (2010); 10.1063/1.3499812

[Order-disorder phase transition and dissociation of hydrogen sulfide under high pressure: Ab initio molecular dynamics study](#)

J. Chem. Phys. **132**, 164506 (2010); 10.1063/1.3392673




[Ab initio molecular dynamics of hydrogen dissociation on metal surfaces using neural networks and novelty sampling](#)

J. Chem. Phys. **127**, 154716 (2007); 10.1063/1.2794338



AIP | The Journal of
Chemical Physics

Meet The New Deputy Editors

	Peter Hamm		David E. Manolopoulos		James L. Skinner
---	-------------------	---	------------------------------	---	-------------------------

On the room-temperature phase diagram of high pressure hydrogen: An *ab initio* molecular dynamics perspective and a diffusion Monte Carlo study

Ji Chen,¹ Xinguo Ren,² Xin-Zheng Li,^{3,4,a)} Dario Alfè,^{5,6,7,b)} and Enge Wang^{1,4,c)}

¹International Center for Quantum Materials, Peking University, Beijing 100871, People's Republic of China

²Key Laboratory of Quantum Information, University of Science and Technology of China, Hefei 230026, Anhui, People's Republic of China

³School of Physics, Peking University, Beijing 100871, People's Republic of China

⁴Collaborative Innovation Center of Quantum Matter, Beijing 100871, People's Republic of China

⁵London Centre for Nanotechnology, University College London, London WC1H 0AH, United Kingdom

⁶Department of Physics and Astronomy, University College London, London WC1E6BT, United Kingdom

⁷Department of Earth Sciences, University College London, London WC1E6BT, United Kingdom

(Received 26 November 2013; accepted 19 June 2014; published online 8 July 2014)

The finite-temperature phase diagram of hydrogen in the region of phase IV and its neighborhood was studied using the *ab initio* molecular dynamics (MD) and the *ab initio* path-integral molecular dynamics (PIMD). The electronic structures were analyzed using the density-functional theory (DFT), the random-phase approximation, and the diffusion Monte Carlo (DMC) methods. Taking the state-of-the-art DMC results as benchmark, comparisons of the energy differences between structures generated from the MD and PIMD simulations, with molecular and dissociated hydrogens, respectively, in the weak molecular layers of phase IV, indicate that standard functionals in DFT tend to underestimate the dissociation barrier of the weak molecular layers in this mixed phase. Because of this underestimation, inclusion of the quantum nuclear effects (QNEs) in PIMD using electronic structures generated with these functionals leads to artificially dissociated hydrogen layers in phase IV and an error compensation between the neglect of QNEs and the deficiencies of these functionals in standard *ab initio* MD simulations exists. This analysis partly rationalizes why earlier *ab initio* MD simulations complement so well the experimental observations. The temperature and pressure dependencies for the stability of phase IV were also studied in the end and compared with earlier results. © 2014 AIP Publishing LLC. [<http://dx.doi.org/10.1063/1.4886075>]

I. INTRODUCTION

Ever since Wigner and Huntington's prediction that pressure-induced metallization might happen in solid hydrogen,¹ understanding the hydrogen phase diagram at megabar pressures has become one of the greatest challenges in condensed matter physics. Besides the possible high T_c superconductivity,^{2,3} this hydrogen under high pressure also serves as a candidate model system for the existence of many interesting states of matter, e.g., the low-temperature superfluid,⁴ and the low-temperature quantum liquid,^{4,5} etc. Recent advances in static diamond anvil cell (DAC) experiments mean that now one can measure properties of hydrogen at pressures of 360 GPa or even higher.⁶⁻⁹ When combined with theoretical simulation techniques, which allow the atomic level structures of this matter to be specifically addressed, the low temperature (150 K and below) phase diagram of hydrogen has been established to a large extent.^{6,7,10-17} Three molecular solid phases (labelled as phases I, II, and III in literature) have been identified in both experimental and theoretical studies. Phase I is an insulating quantum crystal consisting of hydrogen molecules

of disordered bond-vector directions with their centers sitting on a hexagonal close packed lattice.⁶ Although consensus has not been reached regarding the structures of phases II and III, they are also both believed to be insulating.¹²⁻¹⁷ Metallic hydrogen, on the other hand, has only been observed at elevated temperatures in the dynamic shock wave experiments.¹⁸⁻²⁰ As a matter of fact, the high temperature (above 1000 K) phase diagram of hydrogen has largely been established using this technique with assistance from theoretical simulations.¹⁸⁻²⁴ Upon increasing the temperature or pressure, a molecular-to-atomic liquid-liquid phase-transition has been well-characterized. Associated with this change of the nuclear configurations, the system also shows a transition from an insulating to a metallic state for the electronic structures. In between the low-temperature (below 150 K, where the phases are all insulating and molecular) and high temperature (above 1000 K, where the phase is either an insulating or a metallic liquid) regions, experimental and theoretical studies of the hydrogen phase diagram mostly focus on pressures below 200 GPa.²⁵⁻²⁷ A molecular solid-to-liquid phase-transition with a negative slope of the melting curve has been identified between 100 and 200 GPa and phases on both sides of the transition line are insulating.

During the trials of seeking for metallic hydrogen at moderate temperatures, evidence for the stabilization of a new

^{a)}Electronic mail: xzli@pku.edu.cn

^{b)}Electronic mail: d.alf@ucl.ac.uk

^{c)}Electronic mail: egwang@pku.edu.cn

insulating solid phase (phase IV) has been observed above 200 GPa in recent room temperature DAC experiments.^{28–32} Combining the Raman and Synchrotron Infrared Spectroscopy, the boundaries between phase I, phase IV and the low-temperature phase III were determined.^{30–32} Vibrational properties in these studies indicate that this new phase IV is composed by a mixture of strong and weak molecules. Theoretically, *ab initio* structure searching and finite-temperature molecular dynamics (MD) simulations beyond it have separately reported structures with interpenetrating layers of strong and weak molecules.^{33–37} Within the graphene-like weak molecular layer, proton transfer happens and its frequency increases with pressure.³⁰ This is consistent with the experimental observation that the ν_1 Raman full width at half maximum (FWHM) of phase IV is larger than its value in other phases and this width increases with pressure.^{28,29,35}

In spite of this consistence between theory and experiment concerning the properties of this phase IV, some questions which are fundamentally important in its theoretical description remain unanswered, including, e.g., (i) how accurate are the often used functionals within the density-functional theory (DFT) in describing the electronic structures of this phase, and (ii) what will the impact of quantum nuclear effects (QNEs) be? The first question is important because it is well-known in studies of high pressure hydrogen that by going beyond the often used functionals within DFT, the results obtained from the molecular simulations change.^{23,24,38} And for the second question, it has been known for a long time that the QNEs are important for descriptions of the high pressure hydrogen and therefore they should be included in the molecular simulations. This is true in descriptions of the structures in phase III at low temperatures¹⁷ and the bond-vector directions in phases I and II.^{6,17} It is also true for the prediction of the low-temperature quantum liquid hydrogen above 500 GPa, where upon neglecting the QNEs the low-temperature liquid phase does not exist.⁵ An explicit answer to these questions is clearly desirable. Plus, although the existence of this phase IV at room temperature and its boundary with low-temperature phase III reaches a consensus now, the phase diagram of hydrogen at higher temperatures or pressures beyond phase IV is still unclear. This multi-phase co-existence region of phase diagram is important to our understanding of the metallic transition, i.e., how is the insulator-to-metal liquid-liquid phase-transition at high temperatures connected to the solid-solid phase-transitions at low temperatures. Therefore, a delicate study is highly desired.

In this work, we carry out a series of first-principle computer simulations for hydrogen at 200–450 GPa, starting from analysis on the accuracy of the often used *ab initio* methods in describing the electronic structures and the impact of the QNEs on descriptions of the statistical nuclear configurations. Both *ab initio* MD and *ab initio* path-integral molecular dynamics (PIMD) will be used. Using *ab initio* MD, bond making and bond breaking events as well as the thermal effects can be accounted for in a seamless manner based on the forces computed “on the fly” as the dynamics of the system evolves. By going beyond this with *ab initio* PIMD, the QNEs are also accounted for and by com-

paring the results obtained from MD and PIMD, the role of the QNEs can be examined in a very clean manner.^{5,39–44} Concerning the electronic structures, the accuracy of the often used local-density approximation (LDA), Perdew-Burke-Ernzerhof (PBE) exchange-correlation functional, van der Waals density-functional (labelled as vdW-DF in later discussions, using the optB88-vdW functional as an example),^{45–48} hybrid functional HSE06⁴⁹ within DFT, and the random-phase approximation (RPA) method^{50–52} was analyzed, using structures of the system generated from the *ab initio* MD and PIMD simulations. Taking the state-of-the-art DMC results as benchmark,^{53,54} comparisons of the energy differences between structures generated from the MD and PIMD simulations, which give molecular and dissociated hydrogen, respectively, in the weak molecular layer of phase IV, indicate that standard functionals in DFT tend to underestimate the dissociation barrier of the weak molecular layer, with the hybrid HSE06 functional and the RPA method underestimating the least. Because of this underestimation, inclusion of the QNEs in PIMD using electronic structures obtained from functionals like PBE or vdW-DF leads to artificially dissociated hydrogen layers, in clear discrepancy with the experimental observations that this phase IV is a mixed phase composed by both strong and weak molecules. An error cancellation between the neglect of QNEs and the deficiencies of these functionals in standard *ab initio* MD simulations therefore exists, which partly explains why the *ab initio* MD simulations on phase IV reported so far agree so well with the experimental results.^{34–36} In the end, we also analyzed the temperature and pressure dependencies for the stability of phase IV and compared our results with earlier studies.

The paper is organized as follows. In Sec. II, we introduce the methods we have used and the settings of the first-principle calculations. In Sec. III A, we show our results on the structures of phase IV obtained from the *ab initio* MD and PIMD simulations. In Sec. III B, we analyze the accuracy of different *ab initio* electronic structure methods, taking the DMC results as benchmark. How the accuracy of the *ab initio* MD and PIMD simulations is related to the choice of these underlying electronic structures will also be discussed. In Sec. III C, we present some further exploration of the hydrogen phase diagram by focusing on the temperature and pressure dependencies for the stability of phase IV. The conclusions and perspectives are given in Sec. IV.

II. COMPUTATIONAL DETAILS

The first-principle MD and PIMD simulations of the “Born-Oppenheimer-type” were carried out using the plane wave based DFT code VASP.⁵⁵ Projector augmented wave (PAW) potentials along with a 500 eV cutoff energy was employed for the expansion of the electronic wavefunctions. In the MD and PIMD simulations, both PBE⁵⁶ and the optB88-vdW functional within the vdW-DF scheme^{45–48} were chosen. Based on the structures of the system generated from these MD and PIMD simulations, other electronic structure calculations using LDA, hybrid HSE06 functionals within DFT, and the RPA method were also performed with this package.^{49,51,52} A supercell containing 432 hydrogen atoms

and a $(3 \times 3 \times 3)$ Monkhorst-Pack grid were used to sample Brillouin zone in the MD simulations, while in the PIMD and RPA calculations we used a 96 atom supercell and a $(4 \times 4 \times 4)$ MP grid. For the representation of the imaginary time path-integral in the PIMD simulations we have chosen 32 beads per nucleus, whose convergence was seriously checked by comparing with results obtained using 16 and 48 beads. The MD (PIMD) data reported were based on simulations of 10 ps together with a NVT ensemble, whose temperature was controlled using the Nosé-Hoover Chain.⁵⁷

The DMC calculations were performed with the CASINO code,⁵³ using a Dirac-Fock pseudopotential^{58,59} with a core radius of 0.26 Å. We used pseudopotentials to make it simpler to obtain trial wavefunctions from plane wave calculations, which guarantee systematic and unbiased basis set convergence. The quality of this pseudopotential has been systematically tested in our earlier studies, see, e.g., Refs. 60–63. The trial wavefunctions were of the Slater-Jastrow type, with a single Slater determinant, and we used the fixed-node or the fixed-phase approximation. The single particle orbitals were obtained from LDA plane-wave calculations with the PWSCF package,⁶⁴ using a plane-wave cutoff of 300 Ryd, and were re-expanded in B-splines.⁶⁵ The Jastrow factor contains one-body and two-body (electron-electron, U , and electron-nucleus, χ) terms, and is optimized by minimizing the variance of the system with variational Monte Carlo simulations. We obtained a minimum variance of 12.7(2) eV²/electron. Adding a three-body term (electron-electron-nucleus, F) decreases the variance by only $\sim 3\%$. Both the locality approximation (LA)⁶⁶ and the “t-move” scheme due to Casula⁶⁷ were used. The locality approximation is non-variational and therefore can have errors on either side of the true energy. These errors are due, in both cases, to the use of non-local pseudopotentials in combination with the imperfect trial wavefunctions. The simulations with the t-move scheme used a Jastrow factor including the U , χ , and F terms, while for those with the LA we only included the U and χ terms. The Jastrow factor was optimized on one snapshot structure, and then used for all the remaining structures. The DMC time step tests were performed by monitoring the energy difference between two snapshots obtained from the MD and PIMD simulations, respectively, using 96-atom and 768-atom super-cells, sampled with the zone boundary k -point $L = (0.5, 0.5, 0.5)$. To address finite size errors we used the method developed by Chiesa *et al.*⁶⁸ One-body finite size effects were addressed by averaging over different twists \mathbf{k}_i ,⁶⁹ $E_M^{tot} = \sum_{i=1}^M E_i/M$, where E_i was the energy calculated at the \mathbf{k}_i tests. Many-body finite size effects, due to long-range correlations, were addressed using the method based on the electronic structure factor.⁶⁸ To perform these tests we used 96-atom, 768-atom, 2592-atom, and 6144-atom super-cells. Out of interest, we also computed finite size corrections based on the LDA, by evaluating $E_L + \Delta E_{LDA}$, with E_L the raw DMC energy evaluated with the L point only and $\Delta E_{LDA} = E_\infty - E_{111}$, where E_∞ is the LDA energy fully converged with respect to the number of \mathbf{k} -points and E_{111} the LDA energy obtained with just the L point. This type of finite size correction is common practice, and we found that in this case it produced results that were only a few meV/atom away from

the fully converged DMC energy with respect to the number of twists. Results of these tests are given in Sec. III B.

III. RESULTS

A. Structure of phase IV from the *ab initio* MD and PIMD simulations

We start our discussion by looking at the statistical nuclear configurations of phase IV at the classical level. Using the mixed molecular structure with intercalating strong and weak molecular layers of both Pc and Cc symmetry as starting structures,^{33,34} our *ab initio* MD simulations confirm the stability of this mixed molecular phase at 300 K from 210 to 290 GPa (Fig. 1). The weak molecular layer is graphene-like. The centers of the molecules in the strong molecular layer form a slightly distorted hexagonal lattice. If we label these strong and weak molecular layers as G and B layers, respectively, the stacking follows a GBGB periodicity, which is consistent with Refs. 35 and 36. Concerning molecular rotation, in the weak molecular layer the in-plane interaction between neighboring molecules is strong so that the movement of nuclei perpendicular to the layer is suppressed. The hydrogen molecules in the strong layer, on the other hand, can rotate toward out of the plane more freely. The same results obtained from simulations using Pc and Cc structures as starting points indicate that the statistical effects are essential to characterize the finite-temperature structures, and it is these finite temperature properties, instead of the static ones, that should be used to complement experiments.^{35,36}

To better characterize these structures, we plot the pair correlation functions (PCFs) of the strong and weak molecular layers separately in Figs. 2(a) and 2(b), using the data generated from the *ab initio* MD simulations. In these MD simulations, the H₂ bond-length in the strong molecular layer (first peak in Fig. 2(a)) does not change with increasing pressures. In the weak molecular layer, the first two peaks in the PCFs (Fig. 2(b)), representing the intra-molecular

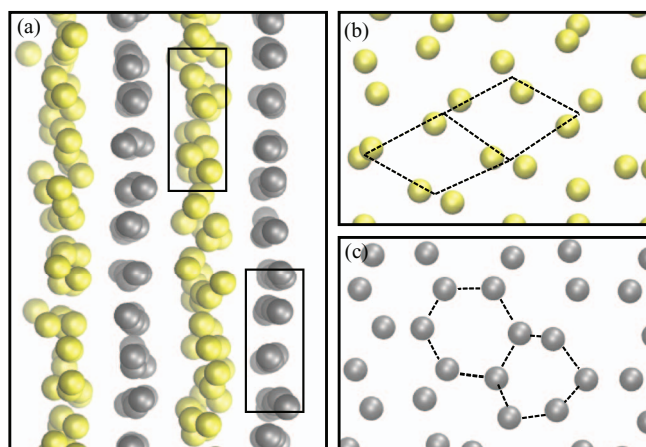


FIG. 1. Snapshots of the *ab initio* MD simulations for the mixed molecular phase. Panel (a) shows the sideview of the simulation cell. Panel (b) shows the topview of the strong molecular layer, as indicated yellow balls in panel (a). Panel (c) shows the topview of the weak molecular layer, as indicated by balls in gray in panel (a). The dashed lines are guide lines for the tetrahedral and honeycomb structures.

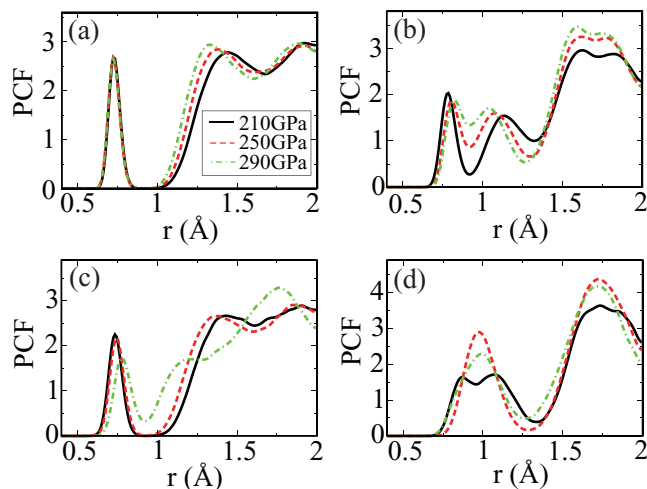


FIG. 2. PCFs of different molecular layers obtained from the *ab initio* MD and PIMD simulations of the mixed molecular phase IV at 300 K. Panel (a): strong molecular layer in the MD simulations. Panel (b): weak molecular layer in the MD simulations. Panel (c): strong molecular layer in the PIMD simulations. Panel (d): weak molecular layer in the PIMD simulations. The legend in panel (a) applies to other panels.

H_2 bond-length and the shortest inter-molecular H–H distance, respectively, are well separated. But they have a tendency to merge into one upon increasing pressures. This is due to an increase of proton transfer rate within the layer,^{35,36} from a few times during the whole simulation, to several times per picosecond. The shift of the first peak to longer distance is consistent with the redshift of the vibration frequency of the weak molecules with increasing pressures in the room temperature Raman experiments.²⁹

Then we turn on the QNEs and look at the results obtained from the *ab initio* PIMD simulations, as shown by the lower two panels in Fig. 2. A fast increase in the H_2 intramolecular bond-length in the strong molecular layer, as reflected by the shift of the first peak in Fig. 2(c) to longer distances, can be observed. Besides this, the clear separation of the first two peaks in the MD simulation of the weak molecular layer (Fig. 2(b)) becomes much less obvious in the PIMD simulation with quantum nuclei at 210 GPa (Fig. 2(d)). And they completely merge into one single peak at 250 GPa and 290 GPa (Fig. 2(d)). In other words, the molecular feature of the weak molecular layer is still kept at 210 GPa upon including the QNEs. At 250 and 290 GPa, however, due to the fact that the protons are totally delocalized upon including the nuclear quantum fluctuations, the graphene-like weak molecular layers become quasi-atomic. Earlier bandgap calculations using structures with these quasi-atomic graphene-like layers suggested that such a system was metallic.^{17,38} In experiments, however, it is well-characterized that this room temperature mixed phase is insulating below 320 GPa.^{29–31} A conflict between theory and experiment therefore exists.

B. Analysis of the electronic structures

To analyze the reason of the “artificial dissociation” of the weak molecules in the PIMD simulations as presented above, we assess the accuracy of the PBE exchange-

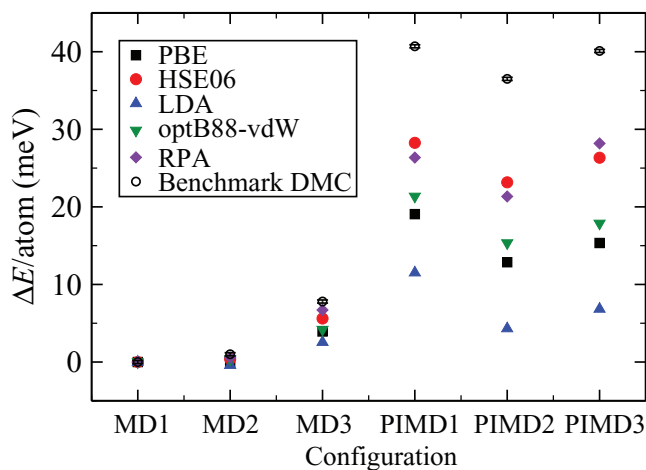


FIG. 3. MD1, MD2, MD3, PIMD1, PIMD2, and PIMD3 are randomly taken snapshots of the nuclei obtained from the *ab initio* MD and *ab initio* PIMD simulations of the mixed phase at 250 GPa and 300 K. The y axis means the total energy difference per atom between those of other snapshots and that of MD1. Since the *ab initio* PIMD simulation (based on PBE exchange-correlation functional) gives quasi-atomic layers in the statically weak molecular layers of the mixed phase, while the *ab initio* simulation preserves such a weak molecular feature, such an energy difference provides a reasonable estimator for the dissociation barrier of the weak molecular layers. The different symbols mean results obtained from different *ab initio* electronic structure calculations. Taking the DMC results as benchmark, it is clear that traditional functionals within DFT give smaller energy differences between those snapshots of the PIMD simulation and those of the MD simulation. Consequently, the dissociation barrier of the weak molecules in the weak molecular layer should be underestimated.

correlation functional used in these simulation, as well as other electronic structure calculation methods, such as the LDA, the optB88-vdW functional within vdW-DF,^{45–48} the hybrid HSE06,⁴⁹ and the RPA method,^{51,52} taking the state-of-the-art DMC results as benchmark. A series of snapshots at the equilibrium state of our MD and PIMD simulations were taken out and the total energies of the system at these configurations were calculated using these different methods. Since the PIMD simulations give a quasi-atomic feature for the weak molecular layers and the MD simulations give us proper weak molecules, the difference between the total energies calculated using the PIMD and MD structures can be used as an estimator for the dissociation energy barrier. The results are shown in Fig. 3 (250 GPa and 300 K). The LDA calculations give the smallest energy differences between the dissociated hydrogen and the weak molecular hydrogen states. The PBE functional also underestimates this dissociation barrier of these weak molecular layers in phase IV by more than 50%. The optB88-vdW is a little better than PBE. The hybrid functional HSE06 is close to the more expensive and complicated RPA results, which includes not only the exact exchange, but also higher-order correlations. However, it is worth noting that even for these two methods this dissociation barrier is still underestimated by $\sim 25\%$. Therefore, a systematic underestimation of this quantity exists in the theoretical description of the electronic structures using these standard methods. For the PIMD simulations, since the PBE exchange-correlation functional underestimates this dissociation barrier within the weak molecular layer by more than 50%, it is reasonable to expect an “artificial dissociation” of the weak molecules in the PIMD simulations.

The rationalization as presented above is based on analysis of the total energy associated with some snapshots obtained from the *ab initio* MD and PIMD simulations. For a more rigorous confirmation of this mechanism from a statistical perspective, we further performed *ab initio* PIMD simulation using electronic structures generated with optB88-vdW functional within the vdW-DF scheme.^{45–48} From Fig. 3, it is clear that this functional provides slightly larger dissociation barrier for the weak molecular layer as compared with the PBE exchange-correlation functional used in the PIMD simulations in Fig. 2. Therefore, if the mechanism we have mentioned above is correct, i.e., underestimation of the dissociation barrier in the PBE exchange-correlation functional results in “artificial dissociation” of the weak molecular layer, *ab initio* PIMD simulation using electronic structures generated by optB88-vdW should give structures with a different dissociation behavior. A slight tendency toward undissociated state in the weak molecular layers should be expected upon using this functional. As a matter of fact, this simulation confirms exactly such a conjecture. This is shown in Fig. 4, where we compare the PCFs of the strong and weak molecular layers in phase IV obtained from the *ab initio* PIMD simulations using the PBE and optB88-vdW electronic structures. It is clear that when optB88-vdW is used, there was a slight preference toward to the molecular state in layer G, especially at 230 GPa, where *ab initio* PIMD using the PBE exchange-correlation functional already gives a quasi-atomic state. Therefore, the underestimation of proton transfer barrier within the weak molecular layer is responsible for the unrealistic delocalization of proton at 250 GPa and 290 GPa in Fig. 2. For the dissociation of the liquid hydrogen at higher

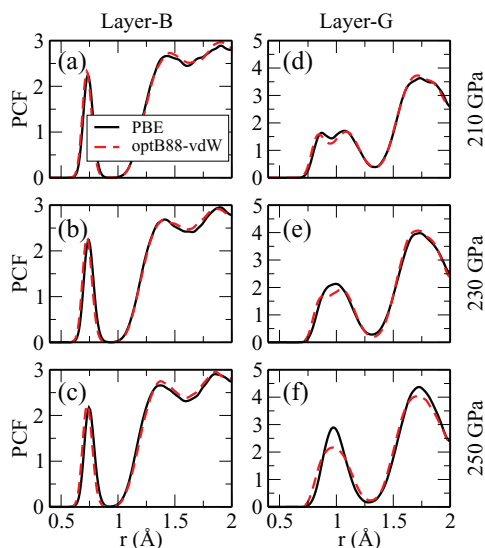


FIG. 4. (a)–(f) PCFs of the strong (labelled as B) and weak (labelled as G) molecular layer in mixed molecular phase from the *ab initio* PIMD simulations using PBE and optB88-vdW for the description of the electronic structures. The temperature is 300 K. The three pressures shown are 210 GPa, 230 GPa, and 250 GPa. The main difference is in the weak molecular layer. When the electronic structures are calculated using optB88-vdW, the weak molecular layer has a slightly larger tendency to keep its molecular feature. This is especially clear in panel (e) (230 GPa), where the molecular layer still keeps its molecular feature in the *ab initio* PIMD simulation using the optB88-vdW electronic structures. While in the *ab initio* PIMD simulation using the PBE exchange-correlation functional, this layer basically becomes atomic.

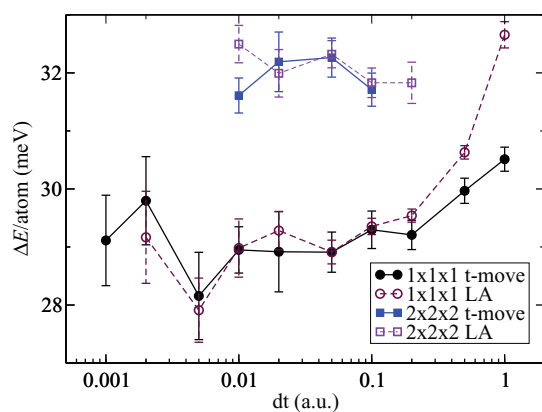


FIG. 5. DMC energy differences (per atom) between two snapshots (MD1 and PIMD3 in Fig. 3) as a function of time step, computed with both the LA and the t-move scheme, using the $1 \times 1 \times 1$ or the $2 \times 2 \times 2$ supercell and the L point.

temperatures, a similar conclusion was drawn in Ref. 23. Here by comparing the total energy differences between the molecular and quasi-atomic states to the benchmark DMC results, we find that similar effects also exist in the theoretical description of phase IV. An error compensation between the neglect of QNEs and the deficiencies of the PBE exchange-correlation functional should be present in the *ab initio* MD simulations as reported in earlier studies.^{34–36}

Concerning the benchmark DMC results, we note that the numbers shown in Fig. 3 are based on supercell simulations containing 768 atoms, 20 twists and a diffusion time step of 0.05 a.u. We take the energy difference ΔE between the snapshots MD1 and PIMD3 in Fig. 3 as an example to show how such parameters were chosen. For the time step tests, both the t-move and the LA schemes were used, and for these particular tests we only used the L point. The results are shown in Fig. 5. We observe that simulations with both the LA and t-move have the same value for ΔE in the limit of zero time step, which indicates that the non-local pseudopotential error is small. The time step dependency of ΔE calculated using both the t-move and the LA schemes is weak, and ΔE is converged within ~ 1 meV/atom up to at least a time step of 0.1 a.u. Then we test finite-size errors using the method developed by Chiesa *et al.*⁶⁸ In Fig. 6, we display ΔE as a function

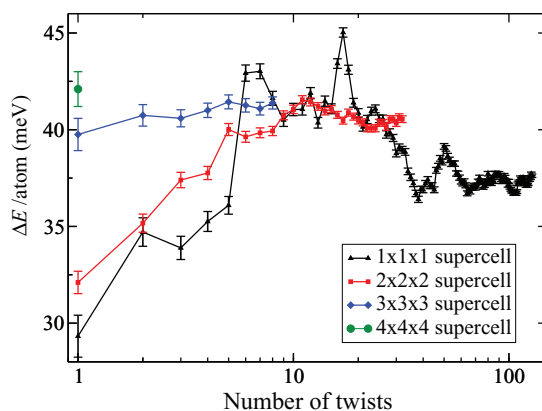


FIG. 6. DMC energy difference (per atom) between two snapshots (MD1 and PIMD3 in Fig. 3) as function of number of twists for the $1 \times 1 \times 1$, $2 \times 2 \times 2$, $3 \times 3 \times 3$, and $4 \times 4 \times 4$ supercells.

of the number of twists, also corrected for many-body size effects. This many-body correction turns out to be the same for the two structures within ~ 1 meV/atom using the $1 \times 1 \times 1$ (96 atoms) supercell, and essentially identical for the two structures for the larger system sizes we tested, and therefore has negligible effects on ΔE . The simulations were performed using $1 \times 1 \times 1$, $2 \times 2 \times 2$, $3 \times 3 \times 3$, and $4 \times 4 \times 4$ supercells, with a time step of 0.05 a.u. The first twist is the L point, and the energy calculated with the fixed-phase approximation is the same (within a statistical error of 0.2 meV/atom) as that computed with the fixed-node approximation, which provides a good cross-check of the internal consistency of the DMC calculations. We note that, because of the different ways of treating moves for walkers near the nodal surface, the fixed-node approximation might have different time step biases than the fixed-phase approximation. In this particular case, however, we have not observed any difference between the two methods. Fig. 6 also shows that this energy difference evaluated with the primitive cells is converged to within a fraction of 1 meV if we use 60 or more twists. The results obtained using a $2 \times 2 \times 2$ supercell show that the energy is converged to well below 1 meV/atom using 20 twists or more, and that this energy is only about 3 meV/atom higher than that obtained with the $1 \times 1 \times 1$ supercell. For the $3 \times 3 \times 3$ supercell, the energy is almost independent from the number of twists, which shows that the energy obtained with the $2 \times 2 \times 2$ supercell is essentially converged. Finally, to complete our finite size tests, we performed one calculation with a $4 \times 4 \times 4$ supercell. Given the very large computational cost of this calculation, we only performed it with the L point and the fixed-node approximation. Remaining finite-size errors with such a big simulation cell are expected to be very small, and indeed the the LDA \mathbf{k} -point correction ΔE_{LDA} is only 0.1 meV/atom. In Fig. 6, we display the result from this calculation, which confirms that the results obtained with the $2 \times 2 \times 2$ supercell are converged to within 2 meV/atom.

C. Further exploration of the phase diagram and speculations

Now we investigate the temperature and pressure dependencies for the stability of the mixed phase. We first acknowledge that in order for this exploration of the phase diagram to be convincing, *ab initio* PIMD simulations based on very accurate electronic structures, better justified by the DMC calculations explicitly for the specific problem to be addressed, should be performed. In the mean time, when melting or the competition between the stability of two solid phases are of interest, some special treatment to get rid of the hysteresis effects or explicit calculations of the free-energy (with anharmonic contributions from both the thermal and the quantum nuclear effects included) must also be taken care. It is fair to say that a rigorous treatment of all these issues is presently beyond the scope of most computational groups. Here, we humbly explore this part of the phase diagram using methods we can afford in our simulations, trying to present some “speculations” on how it is like, with limitations of our simulations explicitly pointed out.

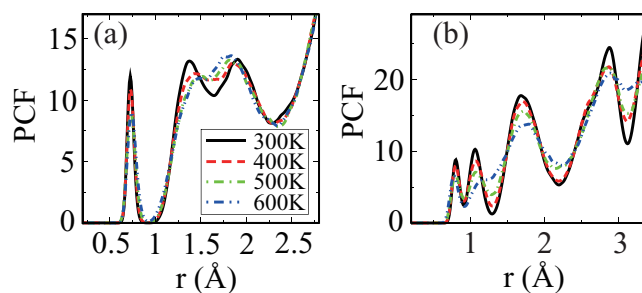


FIG. 7. PCF of the mixed molecular phases at different temperatures within the strong molecular layer (panel (a)) and weak molecular layer (panel (b)). The pressure is ~ 235 GPa. The legend in panel (a) applies to panel (b).

We start by looking at the temperature dependency for the stability of phase IV. The method chosen is *ab initio* MD. When melting is addressed, the two-phase simulation technique is also taken in order to get rid of the hysteresis effects.^{25,70,71} The limitations of these simulations are that they are based on PBE functional within DFT for descriptions of the electronic structures and the classical mechanics for the nuclear motion. However, we note that such a treatment is widely used in practice to explore the phase diagram of hydrogen in earlier studies,^{25,34–37} due to a compensation between computational cost and numerical accuracy. In our *ab initio* MD simulations at $T \geq 300$ K, the structure of this mixed phase IV preserves quite well till melting. This is shown in Fig. 7. As the temperature is raised up from 300 to 600 K, the system is solid, the molecular pair in the strong molecular layer (Fig. 7(a)) persists, and the H–H bond-length does not change. The only effect of raising the temperature is the increment of the bond-length fluctuations. In the weak molecular layer (Fig. 7(b)), however, more stories seem to happen. The intra-molecular bonding of the weak H_2 molecules becomes stronger and stronger as the temperature increases which is reflected by a shift of the first peak in the PCF to shorter distances. In the meanwhile the second peak, corresponding to the shortest inter-molecular distance, starts to disappear, meaning that the graphene-like structure is being destroyed and the mixed molecular phase is likely to melt into a molecular liquid.

For a direct test of this indication, we heated up the system to 800 K. The system melted into a simple molecular liquid with the differences in the weak and strong molecular layers of the mixed phase completely disappeared. We note, however, that this temperature should be much higher than the real melting point due to the existence of the hysteresis effect. To avoid this, as mentioned, we performed two-phase simulations,^{25,70,71} where different starting structures with half solid and half liquid in coexistence were carefully equilibrated (Fig. 8(a)). The principle is that simulations performed at temperatures above (below) the window of the melting temperature result in liquid (solid) phase (Fig. 8(b)). Taking the simulations at 235 GPa as an example, the black line in Fig. 8(b) is the angular integrated PCF of the solid phase (upper inset) at 625 K. This curve corresponds to a typical mixed molecular solid. The red line is the radial distribution function (RDF) of the liquid phase when the same simulation is performed at 650 K, a temperature just above the melt-

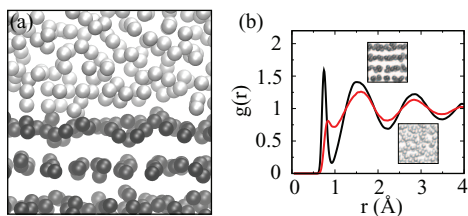


FIG. 8. Panel (a): a snapshot of the starting structure for a two-phase MD simulation. Panel (b): radial distribution function (RDF) of the liquid phase and angular integrated PCFs of the solid phase. The pressure is 235 GPa and temperature is 625 K (black line) or 650 K (red line). The insets show the snapshots of the solid phase (upper inset) and the liquid phase (lower inset) each simulation ended up with.

ing temperature (lower inset). The RDF is characteristic of a liquid phase. A peak at ~ 0.8 Å also suggests that the liquid phase is molecular. It is fair to say that this treatment facilitates us to bracket the lower and upper boundaries of the melting temperature which are shown by the up and down triangles in the phase diagram in Fig. 9. The mixed phase IV melts directly into molecular liquid.

In earlier studies, it was already known that the molecular liquid state arrived at after melting further dissociates into an atomic liquid at even higher pressures and temperatures.^{23,25} As a step further to explore the neighborhood for the stability of the solid phase IV, the molecular liquid, and this atomic liquid states, we performed additional simulations for the melting and the molecular-to-atomic liquid-liquid phase-transitions (LLPT). The melting line was established using the two-phase simulation method as described in the earlier paragraph. Then, we increase the temperature and the molecular liquid disappears and transforms into an atomic liquid. This is shown in Fig. 10(a), where it is clear that at 235 GPa upon increasing the temperature the first peak associated with the intra-molecular H–H bond-length disappears. To precisely locate the position of the dissociation point and identify the feature of this phase-transition, we follow Ref. 23 and simulate the isothermal compression at different temperatures. The RDFs obtained from the simulations at different pressures along the isothermal compression line at 800 K

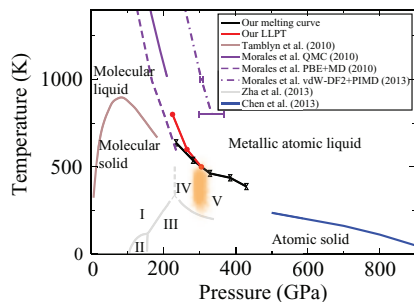


FIG. 9. Phase Diagram of Hydrogen below 950 GPa and 1400 K. Black line and triangles show the melting temperatures and their lower and upper limit from our MD simulation. Red line with circles is the LLPT boundary from our MD simulation. The point when they merge represents the critical point. Melting curve below 200 GPa (brown line) and above 500 GPa (blue line) are from Ref. 74 and Ref. 5. The violet lines show the LLPT transition using different methods in Refs. 23 and 24. Phase boundaries separating I, II, III, and IV phases are from Ref. 31. Orange shadowed region indicates the tendency to transfer from the mixed molecular phase (IV) and to a new one (phase V).

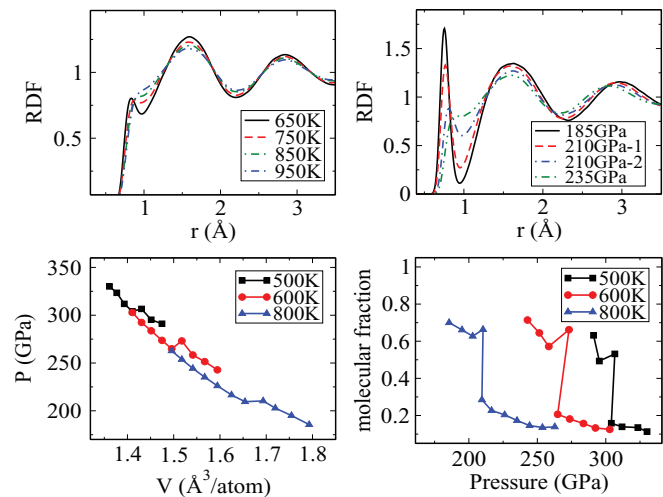


FIG. 10. Panel (a) is the RDF of the liquid phase at different temperatures at 235 GPa. Panels (b)–(d) are results obtained from simulations of the isothermal compression. Panel (b) shows the evolution of the RDFs with pressure at 800 K. Panel (c) shows the isothermal compression curves at 500 K, 600 K, and 800 K. Panel (d) shows the evolution for the fraction of the molecules in the liquid with compression at 500 K, 600 K, and 800 K. From panels (b)–(d), it is clear that the liquid-liquid phase-transition is first-order.

are plotted in Fig. 10(b). At 185 GPa, a sharp peak at ~ 0.75 Å indicates that the liquid is molecular. Upon increasing the pressure, at 210 GPa, two different simulations give a molecular phase (denoted as 210 GPa-1 in Fig. 10) and an atomic phase (denoted as 210 GPa-2 in Fig. 10), respectively. The simulation at 235 GPa gives a clear atomic phase. Therefore, the molecular-to-atomic LLPT is first-order and it happens at 210 GPa when $T = 800$ K. For a more clear representation of this discontinuous feature, we further plot the isothermal compression curves for T equals 500 K, 600 K, and 800 K in Fig. 10(c). By monitoring the cliff of the isothermal compressibility (Fig. 10(c)), we locate the first-order LLPT at 500 K to ~ 305 GPa, at 600 K to ~ 270 GPa, and at 800 K to ~ 210 GPa. This discontinuous feature and the transition points are further confirmed by the evolutions for the fraction of the molecules in the liquid with compression in Fig. 10(d). Such a treatment allows us to determine the molecular-to-atomic LLPT curve, as shown by the red curve in Fig. 9. From this figure, it is clear that the triple point between the solid, molecular liquid, and atomic liquid phases is at 300 GPa and 500 K. In Ref. 25, based on simulations of melting and dissociation at $P \leq 200$ GPa, a triple point has been proposed at 300 GPa and 400 K using linear extrapolation. Here direct simulations for the phase diagram of this region show that this linear extrapolation presents a good estimation. We notice that one difference between our simulations and those in Ref. 25 is that the melting line is simulated using solid phase of different structures. In our case it is the mixed phase IV and in their simulations it was a molecular solid on hexagonal close packed lattice. The most important feature in common, however, is that both are based on *ab initio* MD using PBE functional within DFT for the description of the electronic structures. The similar result obtained indicates that a triple point around here should be present in theoretical simulations with similar methods. Whether this is still true

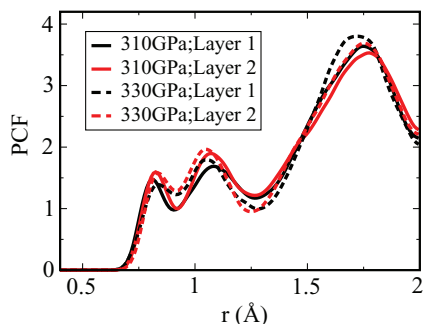


FIG. 11. PCFs of the different molecular layers in the *ab initio* PIMD simulations at 300 K. Black lines: 310 GPa; Red lines: 330 GPa. Layers 1 and 2 mean the originally strong and weak molecular layers, respectively. From this figure, it is clear that the mixed phase IV transfers into a new phase at these pressures with distinctions between the strong and weak molecular layers completely disappear.

in theoretical descriptions using “the” recipe, i.e., *ab initio* PIMD based on very accurate electronic structures, should be a problem of fundamental importance for future studies.

In the end, we explore the pressure dependency for the stability of phase IV. Isothermally, starting from the mixed molecular phase IV at 200 GPa and increasing the pressure to 350 GPa, a phase-transition from the mixed molecular phase (*Pc*) to a weak molecular phase (with *Cmca* symmetry and 4 atoms in the primitive cell) is observed directly in the *ab initio* PIMD simulations. The phase-transition pressure is at ~ 300 GPa, beyond which the strong molecular bonds in mixed phase become weaker, while the weak molecular bonds become stronger. The final structure at above 300 GPa is a layered weak molecular phase (*Cmca*).^{72,73} In Fig. 11, we show the PCFs obtained from the *ab initio* PIMD simulations at 310 GPa and 330 GPa. For clarity, we plot the PCFs from the intercalating layers as we have done in Fig. 2. In the mixed phase IV, these layers correspond to the strong and weak molecular layers, respectively. Therefore, large difference exists between their PCFs. In the equilibrated state we arrived at in these PIMD simulations, however, the difference between even layers and odd layers almost disappears at 310 GPa and 330 GPa. In above discussions, we have shown that the deficiency of the PBE exchange-correlation functional might underestimate the dissociation barrier for the weak molecular layer. In this case, however, the situation is different in the sense that the resulting structure (*Cmca*) is weak molecular in both layers instead of being atomic in one of them. As already mentioned, we completely acknowledge that a rigorous treatment of the phase-transition at this pressure range should resort to *ab initio* PIMD simulations based on more accurate electronic structure calculations, better justified using the DMC results, which is beyond the computational load we can afford nowadays. And in this specific case when the competition between the stability of two solid phases is of interest, explicit calculation of the free-energy (with anharmonic contributions from both the thermal and the quantum nuclear effects included) should be performed. Here, we just speculate that the instability of the mixed phase at increasing pressures indicates that there is a tendency for a solid-solid phase-transition at higher pressures.

IV. CONCLUDING REMARKS

In conclusion, we studied the finite-temperature phase diagram of hydrogen in the region of phase IV and its neighborhood using *ab initio* MD and *ab initio* PIMD as the basic techniques in this paper. Based on the spatial configurations of the nuclei generated from these simulations, the electronic structures were analyzed using methods like different functionals within DFT, the RPA method, and the DMC method. Taking the state-of-the-art DMC results as benchmark, comparisons of the energy differences between structures generated from the MD and PIMD simulations, with molecular and dissociated hydrogens, respectively, in the weak molecular layers of phase IV, indicate that standard functionals in DFT underestimate the dissociation barrier of the weak molecular layers in this mixed phase. Because of this underestimation, inclusion of the QNEs in PIMD based on electronic structures generated from these calculations leads to artificially dissociated hydrogen layers in phase IV. Therefore, an error compensation between the neglect of QNEs and the deficiencies of these functionals in standard *ab initio* MD simulations should exist. Partly because of this error compensation, *ab initio* MD simulations complement the experimental observations of this phase IV pretty well in the earlier studies. Using a combination of these molecular simulation techniques, as well as the two-phase simulation method, the temperature and pressure dependencies for the stability of phase IV were also discussed in the end, with their results compared with those from earlier studies.

ACKNOWLEDGMENTS

J.C., X.Z.L., and E.W. are supported by the National Basic Research Programs of China under Grant No. 2013CB934600, the National Science Foundation of China under Grant Nos. 11275008, 91021007, 11274012, 11174006, and the Open-Lab program (Project No. 12ZS01) of the Key Laboratory of Nanodevices and Applications, Suzhou Institute of Nano-Tech and Nano-Bionics (SINANO), Chinese Academy of Sciences. X.Z.L. would like to thank R. J. Needs, C. J. Pickard, M. I. J. Probert, and A. Michaelides for helpful discussions. The computational resources were provided by the supercomputer TianHe-1A in Tianjin, China. The QMC calculations were performed on the U.K. national facility ARCHER.

¹E. Wigner and H. B. Huntington, *J. Chem. Phys.* **3**, 764 (1935).

²N. W. Ashcroft, *Phys. Rev. Lett.* **21**, 1748 (1968).

³P. Cudazzo *et al.*, *Phys. Rev. Lett.* **100**, 257001 (2008).

⁴E. Babaev, A. Sudbo, and N. W. Ashcroft, *Nature (London)* **431**, 666 (2004).

⁵J. Chen *et al.*, *Nature Commun.* **4**, 2064 (2013).

⁶H. K. Mao and R. J. Hemley, *Rev. Mod. Phys.* **66**, 671 (1994).

⁷P. Loubeyre, F. Occelli, and R. LeToullec, *Nature (London)* **416**, 613 (2002).

⁸C. S. Zha, Z. X. Liu, and R. J. Hemley, *Phys. Rev. Lett.* **108**, 146402 (2012).

⁹L. Dubrovinsky, N. Dubrovinskaia, V. B. Prakapenka, and A. M. Abakumov, *Nature Commun.* **3**, 1163 (2012).

¹⁰E. Goncharov, A. F. Gregoryanz, R. J. Hemley, and H. K. Mao, *Proc. Natl. Acad. Sci. U.S.A.* **98**, 14234 (2001).

¹¹M. Hanfland, R. J. Hemley, and H. K. Mao, *Phys. Rev. Lett.* **70**, 3760 (1993).

- ¹²C. J. Pickard and R. J. Needs, *Nat. Phys.* **3**, 473 (2007).
- ¹³H. Kitamura, S. Tsuneyuki, T. Ogitsu, and T. Miyake, *Nature (London)* **404**, 259 (2000).
- ¹⁴P. Tolédano, H. Katzke, A. F. Goncharov, and R. J. Hemley, *Phys. Rev. Lett.* **103**, 105301 (2009).
- ¹⁵J. Kohanoff, S. Scandolo, S. de Gironcoli, and E. Tosatti, *Phys. Rev. Lett.* **83**, 4097 (1999).
- ¹⁶M. Städele and R. M. Martin, *Phys. Rev. Lett.* **84**, 6070 (2000).
- ¹⁷X. Z. Li *et al.*, *J. Phys.: Condens. Matter* **25**, 085402 (2013).
- ¹⁸S. T. Weir, A. C. Mitchell, and W. J. Nellis, *Phys. Rev. Lett.* **76**, 1860 (1996).
- ¹⁹W. J. Nellis, S. T. Weir, and A. C. Mitchell, *Science* **273**, 936 (1996).
- ²⁰W. Nellis *et al.*, *Philos. Trans. Ser. A-Math. Phys. Eng. Sci.* **356**, 119 (1998).
- ²¹S. Scandolo, *Proc. Natl. Acad. Sci. U.S.A.* **100**, 3051 (2003).
- ²²K. T. Delaney, C. Pierleoni, and D. M. Ceperley, *Phys. Rev. Lett.* **97**, 235702 (2006).
- ²³M. A. Morales, C. Pierleoni, E. Schwegler, and D. M. Ceperley, *Proc. Natl. Acad. Sci. U.S.A.* **107**, 12799 (2010).
- ²⁴M. A. Morales *et al.*, *Phys. Rev. Lett.* **110**, 065702 (2013).
- ²⁵S. A. Bonev, E. Schwegler, T. Ogitsu, and G. Galli, *Nature (London)* **431**, 669 (2004).
- ²⁶S. A. Bonev, B. Militzer, and G. Galli, *Phys. Rev. B* **69**, 014101 (2004).
- ²⁷S. Deemyad and I. F. Silvera, *Phys. Rev. Lett.* **100**, 155701 (2008).
- ²⁸M. I. Eremets and I. A. Troyan, *Nat. Mater.* **10**, 927 (2011).
- ²⁹R. T. Howie *et al.*, *Phys. Rev. Lett.* **108**, 125501 (2012).
- ³⁰M. I. Howie, T. Scheler, C. L. Guillaume, and E. Gregoryanz, *Phys. Rev. B* **86**, 214104 (2012).
- ³¹C. S. Zha *et al.*, *Phys. Rev. Lett.* **110**, 217402 (2013).
- ³²C. S. Zha, R. E. Cohen, H. K. Mao, and R. J. Hemley, *Proc. Natl. Acad. Sci. U.S.A.* **111**, 4792 (2014).
- ³³C. J. Pickard, M. Martínez-Canales, and R. J. Needs, *Phys. Rev. B* **85**, 214114 (2012).
- ³⁴H. Y. Liu, L. Zhu, W. W. Cui, and Y. M. Ma, *J. Chem. Phys.* **137**, 074501 (2012).
- ³⁵H. Y. Liu and Y. M. Ma, *Phys. Rev. Lett.* **110**, 025903 (2013).
- ³⁶A. F. Goncharov *et al.*, *Phys. Rev. B* **87**, 024101 (2013).
- ³⁷I. B. Magdău and G. J. Ackland, *Phys. Rev. B* **87**, 174110 (2013).
- ³⁸M. A. Morales *et al.*, *Phys. Rev. B* **87**, 184107 (2013).
- ³⁹D. Marx and M. Parrinello, *Z. Phys. B* **95**, 143 (1994).
- ⁴⁰D. Marx and M. Parrinello, *J. Chem. Phys.* **104**, 4077 (1996).
- ⁴¹Q. F. Zhang *et al.*, *Phys. Rev. Lett.* **101**, 215902 (2008).
- ⁴²X. Z. Li, M. I. J. Probert, A. Alavi, and A. Michaelides, *Phys. Rev. Lett.* **104**, 066102 (2010).
- ⁴³X. Z. Li, B. Walker, and A. Michaelides, *Proc. Natl. Acad. Sci. U.S.A.* **108**, 6369 (2011).
- ⁴⁴J. Chen *et al.*, *Phys. Chem. Chem. Phys.* **15**, 6344 (2013).
- ⁴⁵J. Klimés, D. R. Bowler, and A. Michaelides, *J. Phys.: Condens. Matter* **22**, 022201 (2010).
- ⁴⁶J. Klimés, D. R. Bowler, and A. Michaelides, *Phys. Rev. B* **83**, 195131 (2011).
- ⁴⁷J. Klimés and A. Michaelides, *J. Chem. Phys.* **137**, 120901 (2012).
- ⁴⁸M. Dion *et al.*, *Phys. Rev. Lett.* **92**, 246401 (2004).
- ⁴⁹J. Heyd, G. E. Scuseria, and M. Ernzerhof, *J. Chem. Phys.* **124**, 219906 (2006).
- ⁵⁰X. Ren, P. Rinke, C. Joas, and M. Scheffler, *J. Mater. Sci.* **47**, 7447 (2012).
- ⁵¹J. Harl and G. Kresse, *Phys. Rev. B* **77**, 045136 (2008).
- ⁵²J. Harl and G. Kresse, *Phys. Rev. Lett.* **103**, 056401 (2009).
- ⁵³R. J. Needs, M. D. Towler, N. D. Drummond, and R. López, *J. Phys.: Condens. Matter* **22**, 023201 (2010).
- ⁵⁴W. M. C. Foulkes, L. Mitáš, R. J. Needs, and G. Rajagopal, *Rev. Mod. Phys.* **73**, 33 (2001).
- ⁵⁵G. Kresse and J. Furthmüller, *Phys. Rev. B* **54**, 11169 (1996).
- ⁵⁶J. P. Perdew, K. Burke, and M. Ernzerhof, *Phys. Rev. Lett.* **77**, 3865 (1996).
- ⁵⁷G. J. Martyna, M. L. Klein, and M. Tuckerman, *J. Chem. Phys.* **97**, 2635 (1992).
- ⁵⁸J. R. Trail and R. J. Needs, *J. Chem. Phys.* **122**, 014112 (2005).
- ⁵⁹J. R. Trail and R. J. Needs, *J. Chem. Phys.* **122**, 174109 (2005).
- ⁶⁰J. Ma, D. Alfè, A. Michaelides, and E. G. Wang, *J. Chem. Phys.* **130**, 154303 (2009).
- ⁶¹J. Ma, D. Alfè, and A. Michaelides, *J. Chem. Phys.* **134**, 134701 (2011).
- ⁶²B. Santra *et al.*, *Phys. Rev. Lett.* **107**, 185701 (2011).
- ⁶³M. J. Gillan, F. R. Manby, M. D. Towler, and D. Alfè, *J. Chem. Phys.* **136**, 244105 (2012).
- ⁶⁴P. Giannozzi *et al.*, *J. Phys.: Condens. Matter* **21**, 395502 (2009).
- ⁶⁵D. Alfè and M. J. Gillan, *Phys. Rev. B* **70**, 161101(R) (2004).
- ⁶⁶L. Mitáš, E. L. Shirley, and D. M. Ceperley, *J. Chem. Phys.* **95**, 3467 (1991).
- ⁶⁷M. Casula, *Phys. Rev. B* **74**, 161102 (2006).
- ⁶⁸S. Chiesa, D. M. Ceperley, R. M. Martin, and M. Holtzmann, *Phys. Rev. Lett.* **97**, 076404 (2006).
- ⁶⁹C. Lin, F. H. Zong, and D. M. Ceperley, *Phys. Rev. E* **64**, 016702 (2001).
- ⁷⁰T. Ogitsu, E. Schwegler, F. Gygi, and G. Galli, *Phys. Rev. Lett.* **91**, 175502 (2003).
- ⁷¹D. Alfè, *Phys. Rev. B* **68**, 064423 (2003).
- ⁷²S. Azadi, W. M. C. Foulkes, and T. D. Kühne, *New J. Phys.* **15**, 113005 (2013).
- ⁷³S. Azadi and W. M. C. Foulkes, *Phys. Rev. B* **88**, 014115 (2013).
- ⁷⁴I. Tamblyn and S. A. Bonev, *Phys. Rev. Lett.* **104**, 065702 (2010).